

Non-abelian plasma instabilities for strong anisotropy

Dietrich Bödeker ^{a1} and Kari Rummukainen ^{b2}

^a *Fakultät für Physik, Universität Bielefeld, D-33615 Bielefeld, Germany*

^b *Department of Physics, University of Oulu, P.O.Box 3000, FI-90014 Oulu, Finland*

Abstract

We numerically investigate gauge field instabilities in anisotropic SU(2) plasmas using weak field initial conditions. The growth of unstable modes is stopped by non-abelian effects for moderate anisotropy. If we increase the anisotropy the growth continues beyond the non-abelian saturation bound. We find strong indications that the continued growth is not due to over-saturation of infrared field modes, but instead due to very rapid growth of high momentum modes which are not unstable in the weak field limit. The saturation amplitude strongly depends on the initial conditions. For strong initial fields we do not observe the sustained growth.

¹bodeker@physik.uni-bielefeld.de

²kari.rummukainen@oulu.fi

1 Introduction

It is an interesting and still open question to what degree the medium created in high energy heavy ion collisions reaches local thermal equilibrium before it falls apart. Results from the RHIC experiments are hinting towards fast thermalization [1]. For sufficiently large collision energy the relevant running coupling is small and this problem can be addressed theoretically in a controlled way using perturbative QCD. Even if a full analytic calculation is not possible one should at least be able to obtain parametric estimates for the thermalization time and the achieved temperature. Remarkably, the solution to this problem has not been found yet.

Due to the non-isotropic expansion the momentum distribution of the produced partons becomes anisotropic³. If the expansion is mostly 1-dimensional along the collision axis, the typical longitudinal momenta become much smaller than the transverse momenta. Anisotropic momentum distributions cause so called plasma⁴ instabilities, *i.e.*, certain long wave gauge field modes grow exponentially so long as their amplitudes are sufficiently small. This is a collective phenomenon which is not visible in the kinetic equation approach used in [3, 4, 5, 6]. It has been argued that this effect, which is well known in plasma physics, will speed up equilibration in heavy ion collisions since the unstable modes tend to make the momentum distributions more isotropic [7].

There are important qualitative differences between QED and QCD plasma instabilities [10]. In both cases the growth of unstable modes is stopped by non-linear effects. In QED this happens when the amplitude of the unstable modes has become so large that they deflect a particle momentum by a large angle within a distance of one wavelength. This corresponds to gauge field amplitudes A of order p/e where p is a typical particle momentum, henceforth called "hard". When the fields become this large they have a dramatic effect on the plasma particles since they instantaneously make the momentum distribution isotropic. In QCD the gauge fields are self-interacting, and the linear approximation already breaks down at much smaller amplitudes $A \sim k/g$ where $k \ll p$ is a characteristic wave vector of an unstable gauge field mode. A crucial question is whether these non-linearities stop the growth of instabilities. In Ref. [8] it was suggested that gluon self-interactions may not saturate the instabilities because the system can "abelianize" so that the unstable modes can grow until they hit the

³For a nice illustration see Fig. 1 of Ref. [16].

⁴Here "plasma" refers to a system of quarks and gluons which is not necessarily in thermal equilibrium, while sometimes the term "quark-gluon-plasma" is reserved for thermalized or almost thermalized systems.

abelian saturation bound $A \lesssim p/g$. The distribution of hard gluons would then quickly become isotropic, and it has been argued [9] that this is sufficient for a hydrodynamic description to be applicable even if there is no local thermal equilibrium.

The question how plasma instabilities in QCD saturate is thus an important one. It can be addressed most cleanly by neglecting both the expansion of the system and the back reaction on the particle momenta. This is sensible because in the weak coupling limit⁵ the expansion is slow compared to the dynamics of the unstable modes and because there is a large scale separation of particle momenta p and the wave-vectors of unstable modes k .

Because the amplitudes of the unstable field modes become large, we are dealing with a non-linear problem and we cannot compute their time evolution perturbatively. So far our qualitative understanding is very limited and one has to rely on lattice simulations. These are possible due to the large occupation numbers which allows one to use the classical field approximation for the infrared fields. In lattice simulations with fields depending only on t and z it was indeed observed [15] that the fields continue to grow rapidly in the non-linear regime. However, 3+1 dimensional simulations [11, 12] indicate that the instabilities are saturated by non-abelian interactions which would mean that their effect is less dramatic than suggested in Ref. [9]⁶. In [14] it was shown that even then the thermalization process *is* affected by plasma instabilities, because the broadening of longitudinal momenta of the particles caused by the unstable modes is more efficient than due to elastic scattering [6].

Most lattice simulations have so far been restricted to moderate anisotropies. In the present article we report on the evolution of instabilities in strongly anisotropic systems. In Sec. 2 we describe the equations and the approximations we use to solve them. The results are discussed in Sec. 4. In Ref. [20] strongly anisotropic plasmas have been considered in a kinematics and with approximations which are quite different from ours.

⁵More precisely, one has to consider not only weak gauge coupling but also sufficiently large times where the system is sufficiently dilute so that the very notion of particles is applicable. In this regime the expansion rate is parametrically small compared to the time scale relevant to the instabilities [6, 10].

⁶For a recent discussion of the role of dimensionality see [13].

2 The setup

Our starting point is the non-abelian Vlasov equations [18, 19]

$$(D_\mu F^{\mu\nu})^a = g \int \frac{d^3p}{(2\pi)^3} v^\nu f^a, \quad (1)$$

$$(v \cdot Df)^a + g v^\mu F_{\mu i}^a \frac{\partial \bar{f}}{\partial p^i} = 0 \quad (2)$$

These are classical equations of motion for SU(2) gauge fields $A_\mu^a(x)$ interacting with particle degrees of freedom. The average distribution of the particles $\bar{f}(\mathbf{p}) \geq 0$ is a gauge singlet, and the leading charged particle density fluctuations are described by adjoint representation distribution functions $f^a(x, \mathbf{p})$. The particles are moving with the speed of light, thus, the 3-velocity is $\mathbf{v} = \mathbf{p}/|\mathbf{p}|$, and (v^μ) is defined as $(1, \mathbf{v})$.

We neglect the back reaction of the soft gauge field A_μ on \bar{f} and also the expansion, so we take $\bar{f}(\mathbf{p})$ to be space and time independent. Neglecting the x^μ -dependence of \bar{f} is justified as long as the expansion rate of the system is small compared to the growth rate of the unstable modes we are interested in. In an isotropic plasma \bar{f} only depends on $|\mathbf{p}|$; here we consider the anisotropic case, but we assume that \bar{f} is invariant when \mathbf{p} is reflected or rotated around the z -axis.

Our equations describe high momentum modes which are treated as classical colored particles and soft gluons which are treated as classical fields. In order for the classical particle approximation to be valid the wave vectors of the fields have to be much smaller than the momenta of the particles. The classical field approximation is valid because we will be dealing with large occupation number (large amplitude) gluon fields. The expansion of the system has been neglected because at weak coupling the expansion rate is much smaller than the rate at which the soft gluons evolve. Furthermore, the back-reaction of the soft fields on the momentum distribution has been neglected here ('hard loop approximation').

The $|\mathbf{p}|$ -dependence of f^a is irrelevant for determining the gluon field dynamics. One only needs the integral

$$W^a(x, \mathbf{v}) \equiv 4\pi g \int_0^\infty \frac{dp p^2}{(2\pi)^3} f^a(x, p\mathbf{v}) \quad (3)$$

Integrating (2) over $|\mathbf{p}|$ we obtain

$$(D_\mu F^{\mu\nu})^a = \int \frac{d\Omega_{\mathbf{v}}}{4\pi} v^\nu W^a \quad (4)$$

$$(v \cdot DW)^a = v^\mu F_{\mu i}^a u^i \quad (5)$$

with

$$u^i(\mathbf{v}) = -4\pi g^2 \int_0^\infty \frac{dp p^2}{(2\pi)^3} \frac{\partial \bar{f}(p\mathbf{v})}{\partial p^i} \quad (6)$$

For isotropic \bar{f} one would have $\mathbf{u} = m_D^2 \mathbf{v}$, and (2) would be the usual hard thermal loop equation of motion. For an anisotropic plasma \mathbf{u} will not simply be proportional to \mathbf{v} . Since we assume \bar{f} to be parity even, \mathbf{u} is parity odd.

As in [21] we expand $W(x, \mathbf{v})$ in spherical harmonics,

$$W(x, \mathbf{v}) = \sum_{l=0}^{L_{\max}} \sum_{m=-l}^l W_{lm}(x) Y_{lm}(\mathbf{v}) \quad (7)$$

with a finite l -cutoff L_{\max} . This turns Eqs. (4), (5) into classical equations for fields living in 3+1 dimensions. Similarly we expand \bar{f} in spherical harmonics and we assume that it only depends on \mathbf{p}^2 and p_z^2 . Then

$$\bar{f}(\mathbf{p}) = \sum_{l=0}^{L_{\text{asym}}} \bar{f}_l(|\mathbf{p}|) Y_{l,0}(\mathbf{v}) \quad (8)$$

where the sum runs over even l only. In general the l -cutoff L_{asym} would be infinite, but in practice we must choose parametrizations with finite L_{asym} since the equations of motion limit $L_{\text{asym}} \leq L_{\max}$. When we increase L_{asym} it becomes possible to describe more anisotropic distributions, but at the same time L_{\max} and correspondingly memory- and cpu-time requirements of the simulations are increased (roughly proportionally to L_{\max}^2).

The equations of motion in terms of W_{lm} in temporal gauge $A_0 = 0$ become

$$\partial_0 W_{lm} + C_{lm, l'm'}^i D^i W_{l'm'} = F_{0i} u_{lm}^i + 2F_{iz} u_{lm}^{iz} \quad (9)$$

$$\partial_0 F^{0i} + D_k F^{ki} = v_m^i W_{1m}. \quad (10)$$

Gauss law reads

$$D_i F^{i0} = \frac{1}{\sqrt{4\pi}} W_{00}. \quad (11)$$

Here $E^i = -F^{0i}$ is the canonical momentum of the gauge field A^i .

The coefficients $C_{lm,l'm'}^i$ may be found in Appendix A of Ref. [21]. The other coefficients are

$$v_m^i = \int \frac{d\Omega}{4\pi} Y_{1m} v^i, \quad u_{lm}^i = \int d\Omega Y_{lm}^* u^i, \quad u_{lm}^{ij} = \frac{1}{2} \int d\Omega Y_{lm}^* (v^i u^j - v^j u^i). \quad (12)$$

We now define

$$m_l^2 \equiv 4\sqrt{\pi} g^2 \int_0^\infty \frac{dpp}{(2\pi)^3} \bar{f}_l(p) \quad (13)$$

For an isotropic system m_0^2 equals the Debye mass squared. We want \bar{f} to be positive which gives the condition $\sum_l m_l^2 Y_{l0}(\mathbf{v}) \geq 0$ (Albeit we shall violate this condition slightly.).

The only non-vanishing u -coefficients in Eq. (9) are

$$u_{l1}^x = -\frac{\sqrt{\pi}}{2} \frac{\sqrt{l(l+1)}}{\sqrt{2l+1}} \left(\frac{l+1}{\sqrt{2l-1}} m_{l-1}^2 + \frac{l}{\sqrt{2l+3}} m_{l+1}^2 \right) \quad (14)$$

$$u_{l,-1}^x = -u_{l1}^x, \quad u_{l1}^y = u_{l,-1}^y = -iu_{l1}^x \quad (15)$$

$$u_{l0}^z = \sqrt{\pi} \frac{l(l+1)}{\sqrt{2l+1}} \left(\frac{m_{l-1}^2}{\sqrt{2l-1}} - \frac{m_{l+1}^2}{\sqrt{2l+3}} \right) \quad (16)$$

$$u_{l1}^{xz} = \frac{\sqrt{\pi}}{4} \sqrt{l(l+1)} m_l^2 \quad (17)$$

$$u_{l,-1}^{xz} = -u_{l1}^{xz}, \quad u_{l1}^{yz} = u_{l,-1}^{yz} = -iu_{l1}^{xz} \quad (18)$$

We study the behavior of the system using both weakly and strongly anisotropic distributions. A measure of the anisotropy is

$$\eta^2 \equiv 3 \langle v_z^2 \rangle / \langle \mathbf{v}^2 \rangle, \quad (19)$$

which equals 1 for symmetric and 0 for completely planar distribution.

For each L_{asym} the distribution is parameterized by the coefficients m_l^2 , with $l = 0, 2, \dots, L_{\text{asym}}$. The values of m_l^2 are chosen so that the anisotropy of the resulting

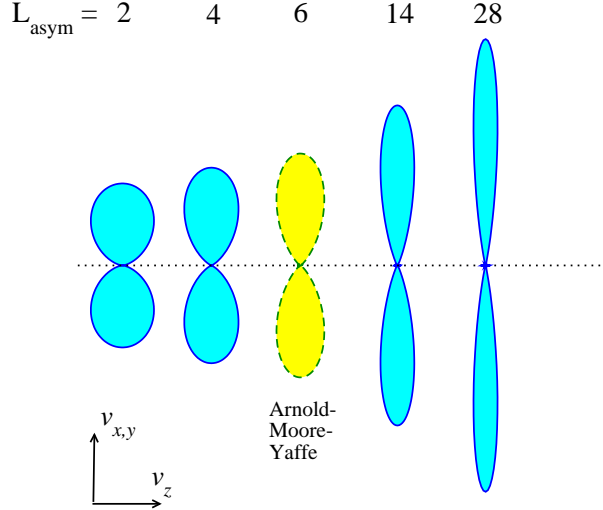


Figure 1: Anisotropic hard particle distributions used in this work, together with the distribution used by Arnold, Moore and Yaffe [11]. The distributions are plotted so that the relative number of particles moving to direction \mathbf{v} is proportional to the length of the radial vector from the center of the plot. For each L_{asym} we tried to maximally localize the distribution in the xy -plane. The distributions are normalized to equal area for readability.

distribution is approximately maximized. The reason for this choice is that for a given anisotropy, we take L_{asym} as small as possible, also minimizing the required L_{max} and hence computational requirements.

For $L_{\text{asym}} = 2$ and 4 the tuning of the parameters is easy enough to do by hand, but for $L_{\text{asym}} = 14$ and 28 we use a 1-parameter fitting procedure: $\bar{f}(\theta)$ is fitted to a narrow Gaussian function centered at $\theta = \pi/2$. The width of the Gaussian is adjusted to be as small as possible while still giving a good fit; if the width of the Gaussian is too small the fitted function will have large oscillations over whole θ -range. The quality of the fit is justified by eye. This procedure is sufficient for our purposes: the goal is to find one good enough parametrization for the asymmetry, and no attempt is made to maximize the asymmetry for any given L_{asym} . The resulting parameters are given in table 1.

This process gives distributions where the power is strongly concentrated around $\theta = \pi/2 \pm \Delta\theta$, where $\Delta\theta$ is the maximum resolution power of the Y_{l0} -expansion when $l \leq L_{\text{asym}}$, that is $\Delta\theta \sim \pi/L_{\text{asym}}$. Thus, when plotted on cartesian coordinates, the distribution has well-defined “lobes” centered around direction $\theta = \pi/2$, i.e. along the

L_{asym}	2	4	14	28
η^2	0.6	0.4	0.086	0.022
m_2^2/m_0^2	-0.447	-0.671	-1.021	-1.093
m_4^2/m_0^2		0.167	0.833	1.046
m_6^2/m_0^2			-0.603	-0.967
m_8^2/m_0^2			0.390	0.867
m_{10}^2/m_0^2			-0.227	-0.756
m_{12}^2/m_0^2			0.119	0.640
m_{14}^2/m_0^2			-0.057	-0.526
m_{16}^2/m_0^2				0.421
m_{18}^2/m_0^2				-0.327
m_{20}^2/m_0^2				0.247
m_{22}^2/m_0^2				-0.181
m_{24}^2/m_0^2				0.130
m_{26}^2/m_0^2				-0.090
m_{28}^2/m_0^2				0.061

Table 1: The parameters m_l^2 used in simulations. $L_{\text{asym}} = 2$ and 4 correspond to weak asymmetry, $L_{\text{asym}} = 14$ and 28 to strong asymmetry.

xy -plane, as shown in Fig. 1. For directions near $\theta \approx 0$ or π , the distributions can become slightly negative; however, the magnitude of this effect is negligible.

For small amplitudes the non-linear terms in the equations of motion can be neglected. Modes with different wave vectors do not mix, and the unstable modes grow exponentially at a rate which can be calculated analytically. The growth rate is shown in Fig. 2 as a function of the length of the wave vector of the unstable mode for different asymmetries. For each asymmetry k_* denotes the value of $|\mathbf{k}|$ for which the growth rate is maximal. For the smallest to the largest anisotropy, the maximum growth rate increases by a factor of 5 and the width of the unstable mode distribution by a factor of 8.

The linear equations of motion offer a straightforward method for investigating how large we need need to make L_{max} in order to reproduce the continuum dynamics. In Fig. 3 we compare the growth rate at $L_{\text{max}} = \infty$ with the rates at different finite values of L_{max} for modes with $\mathbf{k} = k\hat{\mathbf{z}}$. For weak anisotropy ($L_{\text{asym}} = 2$, left figure) one needs rather large values of $L_{\text{max}} \gg L_{\text{asym}}$ to reproduce the growth rate. The growth rate for strong anisotropy $L_{\text{asym}} = 28$ (right figure) can be reproduced already with $L_{\text{max}} \gtrsim L_{\text{asym}}$. Indeed, for the asymmetries used in this study it appears that the finite

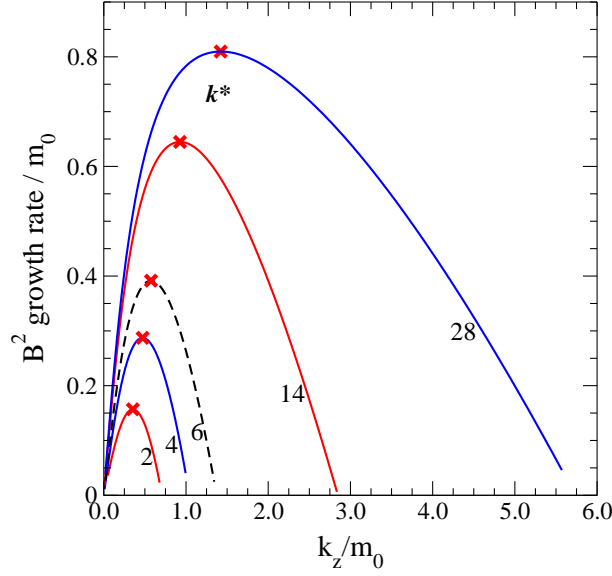


Figure 2: Soft field growth rate as a function of momentum $\mathbf{k} = k\hat{\mathbf{z}}$ for linearized equations of motion, for anisotropic hard mode distributions $L_{\text{asym}} = 2, 4, 6, 14$ and 28 (see Fig. 1 and table 1). k_* is the wave number with the maximal growth rate.

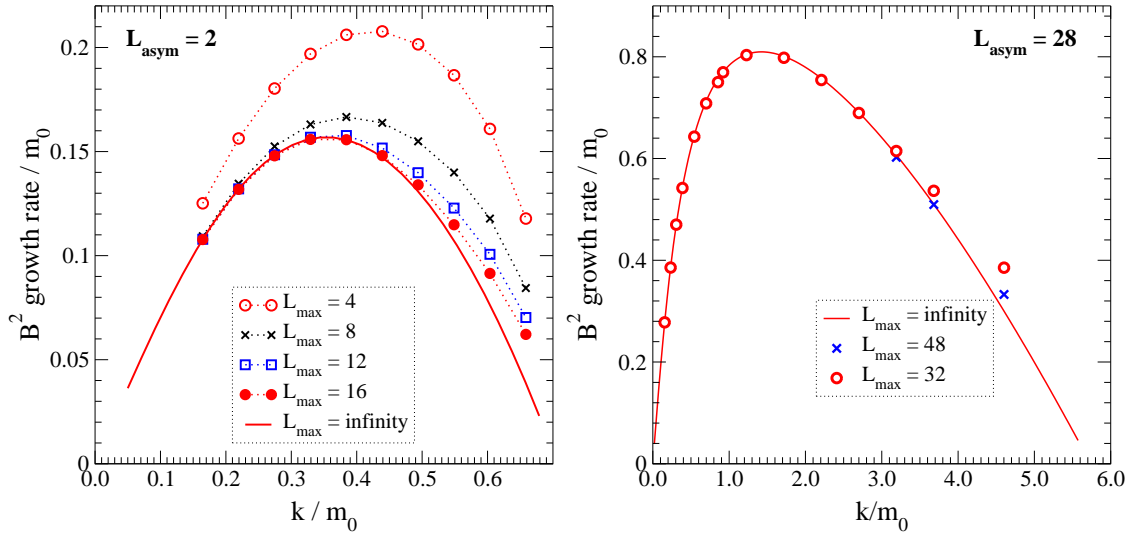


Figure 3: Growth rate of magnetic energy for the linearized equations of motion with different L_{max} cutoffs, shown for $L_{\text{asym}} = 2$ (left) and $L_{\text{asym}} = 28$ (right).

L_{\max} effects are roughly independent of the L_{asym} used, and we should obtain accurate results for $L_{\max} \gtrsim 16$, of course provided that we keep $L_{\max} > L_{\text{asym}}$. In Sec. 5 we investigate the L_{\max} -dependence of the real simulations in detail.

We note that while the rate can be solved analytically at finite L_{\max} , in Fig. 3 we actually measured the rate from numerical simulations using a linearized version of our simulation program. Thus, this measurement was also an important check of the correctness of the simulation program.

3 Simulation program and parameters

The equations of motion (9), (10) are discretized as described in Ref. [21]; we invite interested readers to check therein for the detailed implementation. We note that we implement the W -fields in a “staggered” fashion: because the W equations of motion only have first order derivatives, a symmetric discretization decouples W -fields at even and odd lattice sites from each other (i.e. at space-time sites where the integer coordinate $n_x + n_y + n_z + n_t$, where n_t is the number of the evolution time step, is either even or odd.). Thus, we can delete the W -field at odd sites, saving memory and cpu-time.⁷

For the time update we use a time-symmetric staggered leapfrog as described in [21]. The only essential difference is the appearance of the last term in Eq. (9). In order to guarantee that the update remains invariant under time reversal we implement the update of the W -fields in two stages, interleaving these with the gauge and electric field update steps.

The time-step values we use are $\delta t = 0.05a$ and $0.1a$, where a is the spatial lattice spacing. We shall discuss the lattice artifacts – finite a , finite volume, finite δt , and finite L_{\max} – in detail in Sec. 5; to summarize, all lattice effects appear to be well under control.

We note that while all m_l^2 are dimensionful in the equations of motion, for fixed asymmetry the ratios m_l^2/m_0^2 remain constant. Thus, every dimensionful quantity can be given in terms of the powers of single parameter, m_0^2 . In particular the lattice spacing is given as (am_0) . The gauge coupling constant g^2 can be completely absorbed in the equations of motion, making the results independent of the value of g^2 .

⁷This procedure also deletes half of the unphysical doublers inherent in the W -field spectrum. The reason these doublers appear is the same as for the notorious lattice fermion doublers, namely the first order derivatives. However, in our case the doublers are quite benign, as is discussed in [21].

$m_0 a$	$L_{\text{asym}} = 2, L_{\text{max}} = 16$	$L_{\text{asym}} = 4, L_{\text{max}} = 16$
1	64^3	64^3
0.77	64^3	64^3
0.55	$64^3, 80^3, 104^3, 120^3$	$64^3, 128^3$
0.45	$64^3, 120^3$	160^3
$m_0 a$	$L_{\text{asym}} = 14, L_{\text{max}} = 16$	$L_{\text{asym}} = 28, L_{\text{max}} = 32$
1	64^3	48^3
0.77		64^3
0.71	$64^3_{16,24}$	
0.55	$48^3, 64^3_{16,24}, 96^3, 128^3$	64^3
0.32	$64^3_{16,24}, 80^3, 96^3, 120^3_{16,24,32}, 180^3$	
0.30		$64^3, 96^3, 128^3_{32,48}, 192^3$
0.17	240^3	180^3
0.10	240^3	240^3

Table 2: The lattice spacings (in units of m_0) and lattice sizes used in the weak initial field analysis for each value of the asymmetry. For several of the volumes there are more than one individual run. The L_{max} -cutoff used is shown at the top of the columns. In addition, there are some volumes with more than one L_{max} -cutoff; these are indicated with a subscript (only for $L_{\text{asym}} = 14, 28$).

Our initial conditions are as follows: we initialize the electric field components $\mathbf{E}^a(\mathbf{x})$ to a small amplitude white noise, i.e. random Gaussian fluctuations, with vanishing initial \mathbf{A} and W_{lm} . We make an orthogonal projection of the E -fields to a hypersurface satisfying Gauss' law, $D_i E^i = 0$ (since $W_{00} = 0$). The evolution equations preserve Gauss' law. The electric field drives the gauge field \mathbf{A} to a non-zero value very quickly, so that $\langle \mathbf{B}^2 \rangle \approx \langle \mathbf{E}^2 \rangle$ before the exponential growth of the unstable modes becomes visible. The amplitude of the initial fluctuations is chosen small enough so that the equations of motion are essentially linear during the initial stage. The growth of unstable modes then drives the fields to much larger values.

The lattice spacings and sizes used in the analysis are shown in table 2. The simulations have been performed mostly using pc-clusters with infiniband interconnects. The simulations require unusually large amounts of memory (for lattice simulations); our largest simulations used 192 nodes, with a total memory requirement of around 400 GB. The simulations were performed at the Finnish IT Center for Science (CSC).

4 Results

4.1 Energy densities

As mentioned in Sec. 3, the initial condition we use is a white noise spectrum satisfying Gauss' law for the electric field, with \mathbf{A} and W set to zero. In Fig. 4 we show the field evolution for weak anisotropy ($L_{\text{max}} = 2, 4$) starting from very small amplitude initial conditions for different values of the lattice spacing. We see qualitatively the same behavior as observed in Refs. [11, 12]. After some initial settling down, the soft fields start to grow exponentially until they reach the non-abelian point $\mathbf{A} \sim \mathbf{k}/g$ where non-linear terms in the equation of motion start playing a role. We find that this happens when the magnetic field squared approximately equals

$$\frac{1}{2}B_{\text{non-abelian}}^2 \simeq \frac{k_*^4}{4g^2}. \quad (20)$$

After that the growth slows down significantly and is no longer exponential. According to Arnold and Moore [16] this growth is due to cascading of energy from the originally unstable infrared modes to higher momentum ones. The amplitude of the initial fields was not specifically tuned to be equal for different lattice spacings; nevertheless, the gauge field evolution falls on a curve independent of the lattice spacing (as long as the volume is large enough, see Sec. 5). The origin of time $t = 0$ has been adjusted in Fig. 4 in order for the growth phases to overlap. Thus, only differences of t have a physical meaning.

For strong anisotropies we find a very different picture. In Fig. 5 we show our results for $L_{\text{asym}} = 14$ and 28. We clearly see the onset of non-linear effects at the magnetic field energy density around $k_*^4/(4g^2)$. There the growth ceases to be exponential and the dynamics becomes very complicated. The electric field grows very rapidly, and the electric field energy becomes as large as the magnetic one. Subsequently, however, the growth of energy continues at a large rate. It is not a purely exponential growth, but it is not much slower than the initial weak field growth. For $L_{\text{asym}} = 28$ the growth rate is roughly as large as in the weak field regime ($m_0 t < 40$).

At some value of the energy density the growth saturates. Furthermore, in contrast to the moderate asymmetry in Fig. 4, the electric and magnetic field energies reach an equal level at the end. In Fig. 5 we show the values where the growth finally saturates for different values of the lattice spacing a . We see that the saturation energy has a strong dependence on the lattice spacing, growing as am_0 is decreased. Therefore we can conclude that the saturation seen in Fig. 5 is caused by the lattice regularization.

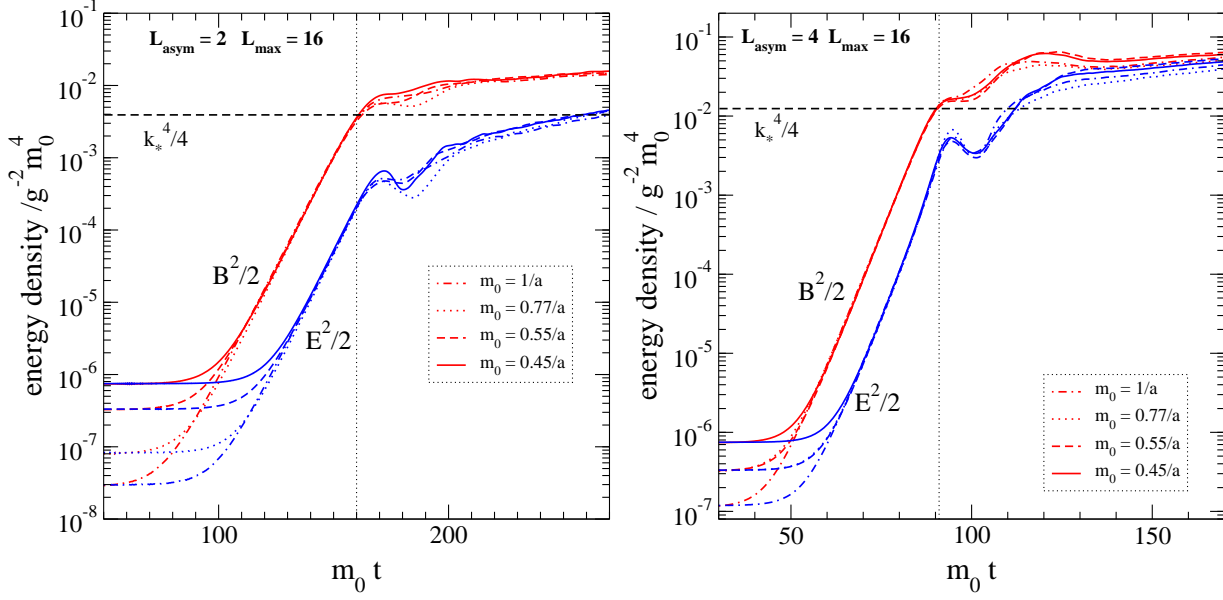


Figure 4: Magnetic and electric field energy densities as a function of time for moderate anisotropy, measured from lattices with different lattice spacings a . The lattice sizes are the largest ones for each lattice spacing in table 2.

In Fig. 6 we show the maximal magnetic energy density as a function of the lattice spacing. The maximal energy density appears to grow without bound with decreasing a with a power-like behavior. The magnetic field energy on the lattice is given by $4/(ag^2) \sum_{i<j} (1 - \frac{1}{2} \text{Tr } U_{ij})$, where U_{ij} is the ordered product of link variables around a spatial plaquette,

$$U_{ij}(x) \equiv U_i(x)U_j(x + a\hat{\mathbf{i}})U_i^\dagger(x + a\hat{\mathbf{j}})U_j^\dagger(x). \quad (21)$$

There is an absolute upper limit on the magnetic energy density, $24/(a^4 g^2)$ which is reached when $\text{Tr } U_{ij} = -2$. This is a very particular fully ordered state; a more realistic limit is the completely random state where $\langle \text{Tr } U_{ij} \rangle = 0$ and where the magnetic energy density reaches the limit $12/(a^4 g^2)$. Energies above this limit are shown in Fig. 6 as a shaded region.

We observe that our maximal field energies do not quite reach the maximum energy limit. Instead, the saturation energy density appears to diverge in the continuum limit with a different power of a . If we fit a power law behavior to the saturation energy density at both asymmetries, we obtain the results $E_{\text{saturation}} \propto (am_0)^{-2.4}$ for $L_{\text{max}} = 14$ and $(am_0)^{-3.2}$ for $L_{\text{max}} = 28$. Because we do not have proper statistical errors for the

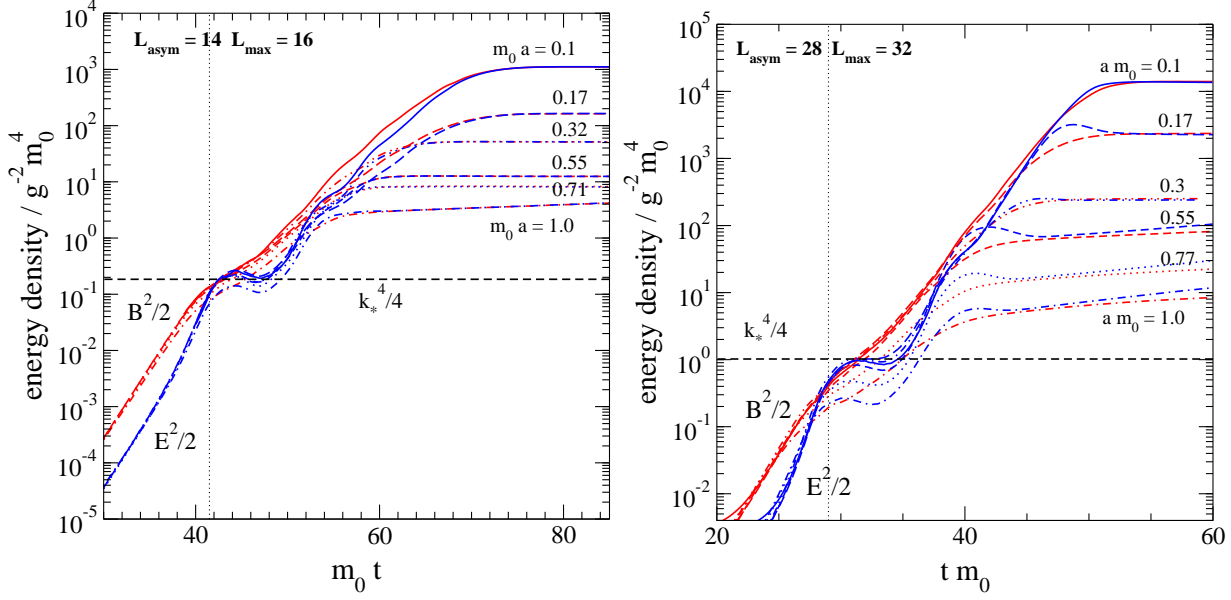


Figure 5: Same as Fig. 4 but for stronger anisotropy. Now the growth of field energy appears to continue indefinitely and it is stopped only by lattice cutoff effects. For each lattice spacing we show the largest volume listed in table 2.

data in Fig. 6, we cannot quote proper error bars for the fitted exponents. However, we can nevertheless make a rough estimate of them by performing jackknife analysis in terms of the individual simulation points, obtaining an error bar ± 0.2 for both exponents. It is worth noting that the exponent in the $L_{\text{asym}} = 28$ case is close to -3 , the exponent given by the thermal distribution with a lattice cutoff.

This analysis shows that there appears to be no saturation of the energy density if the lattice spacing is removed. This is very different behavior from the one that was observed in the 3+1 dimensional simulations of Refs. [11, 12].

Let us now discuss possible reasons for this behavior. When the anisotropy is mild, the unstable modes have momenta of order m_0 . However, for strong anisotropy there are unstable modes with $|k_\perp| \lesssim m_0$ but with longitudinal momentum $|k_z|$ all the way up to k_{max} , where

$$k_{\text{max}} \sim \frac{m_0}{\eta} \quad (22)$$

and η is the measure of anisotropy introduced in eq. (19). In [23] it was argued that the magnetic field squared of these modes cannot become larger than $\mathbf{B}^2 \sim m_0^4/(g^2\eta^2)$.

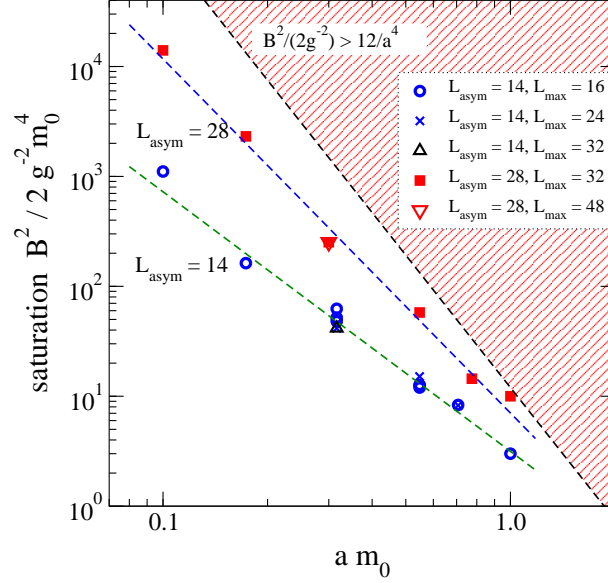


Figure 6: Maximal magnetic field energy density as a function of the lattice spacing for $L_{\text{asym}} = 14$ and 28, and for all values of L_{max} used. The shaded region is above the maximum magnetic field energy density, given by a completely random lattice gauge system. The dashed lines are power-law fits to the two asymmetries, with the results $(am_0)^{-2.4}$ ($L_{\text{asym}} = 14$) and $(am_0)^{-3.2}$ ($L_{\text{asym}} = 28$).

The energy density at saturation in a strongly anisotropic plasma would then be enhanced by a factor $1/\eta^2$ compared to the case of moderate anisotropy. However, this enhancement factor is only about 16 for $L_{\text{asym}} = 14$ and about 67 for $L_{\text{asym}} = 28$, while we see the energy density in Fig. 5 growing by many orders of magnitude larger than in the case of weak anisotropy. Therefore it is not a (quasi-) exponential growth of modes whose equations of motion are almost linear which could explain the behavior seen in Fig. 5. Thus the continued growth must be an effect which is essentially non-linear.

There appear to be (at least) two scenarios for the physics behind the continued growth. The first is that the unstable modes grow to occupancy much larger than $1/g^2$ as suggested in Ref. [8]. Another possibility is that the energy goes into the high momentum modes, rather than into the modes which are unstable in the weak field regime. We shall try to distinguish between these outcomes by measuring quantities which are sensitive to the momentum spectrum of the gauge fields: gauge fixing and direct Fourier transformation, gauge invariant operators and gauge invariant cooling. These all indicate that the energy indeed gets dumped to the UV, and there is no

growth of the IR modes much beyond the non-abelian point.

4.2 Coulomb gauge occupation numbers

For free gluon fields the concept of occupation numbers $f_s(\mathbf{k})$ ⁸ is unambiguous. It can be calculated from the gauge field by fixing to Coulomb gauge using the expression

$$f_s(\mathbf{k}) = \frac{|\mathbf{k}|}{2VN_{\text{dof}}} \left| \mathbf{A}(\mathbf{k}) - \frac{i}{|\mathbf{k}|} \mathbf{E}(\mathbf{k}) \right|^2 \quad (23)$$

where N_{dof} denotes the number of color/spin degrees of freedom. For reflection invariant field configurations the interference term of \mathbf{A} and \mathbf{E} vanishes. For free fields the two remaining terms give equal results when they are averaged over time. Thus, assuming reflection invariance, one can compute the occupancy either from \mathbf{A} or from \mathbf{E} only, and in this work we use the former case. The distributions shown here are averaged over all directions of \mathbf{k} ,

$$f(k) \equiv \int \frac{d\Omega}{4\pi} f_s(\mathbf{k}) \quad (24)$$

If the gluon field amplitudes are large and/or the gluons are interacting with the particles, there is no occupation number in the strict sense. Nevertheless one expects that (23) still gives a good estimate of the power in one field mode. However, fixing the gauge for large fields in a non-abelian theory is dangerous due to Gribov copies of near vacuum configurations of the high momentum modes. We make three consistency checks of the gauge fixed spectrum by comparing with gauge invariant measurements: the total energy in the gauge fixed spectrum, measurement of the average $\langle \mathbf{k}^2 \rangle$, and comparing the spectrum with gauge invariant cooling. These will be discussed below.

The occupation numbers as a function of time are shown in Fig. 7, for strong ($L_{\text{asym}} = 28$) and moderate anisotropy ($L_{\text{asym}} = 4$). The curves show the spectrum measured at constant evolution time intervals. Early times are at the bottom; the initial white noise \mathbf{E} -field implies a spectrum $f(k) \sim 1/k$.

Let us first consider the case of strong anisotropy. At early times one sees a rapid growth of the infrared modes which is the fastest at $k = k_*$. The dashed curve is at the time at which non-linear effects become important. In Fig. 5 this time is marked with a vertical dotted line. As this is happening the active mode spectrum widens very rapidly.

⁸We use the subscript s to distinguish the occupation number of the classical (soft) fields from the occupation number of hard gluons which are described by the W -field.

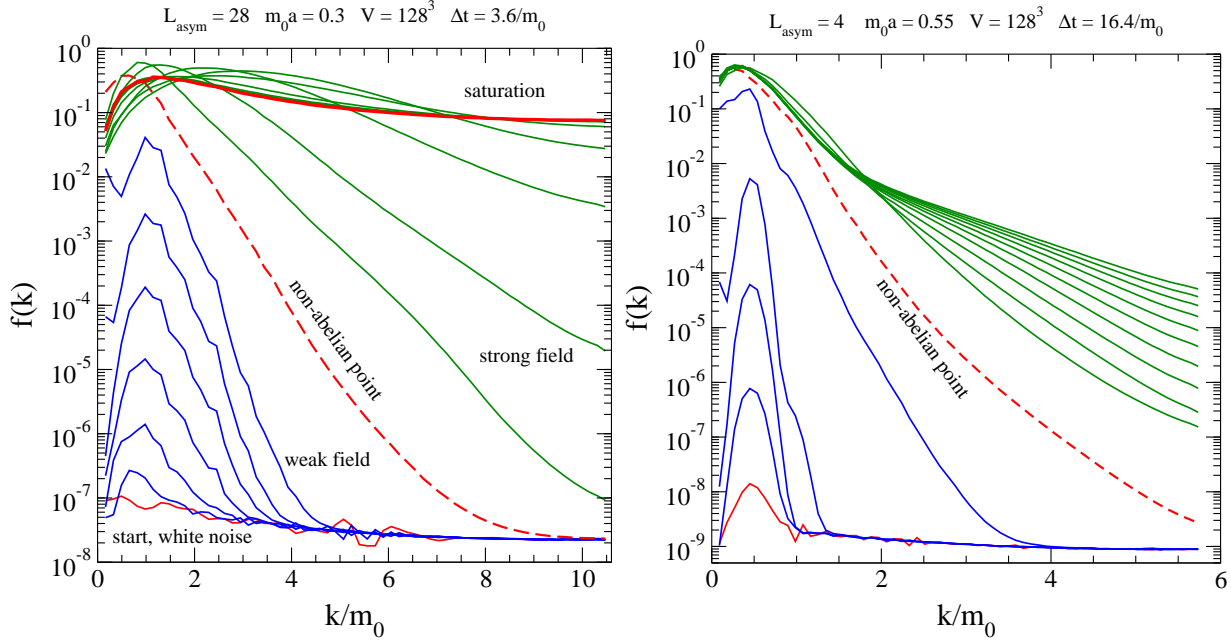


Figure 7: Coulomb gauge power spectrum (occupation number) as a function of time for strong ($L_{\text{asym}} = 28$, left) and weak ($L_{\text{asym}} = 4$, right) anisotropy. The power spectra are plotted at equal intervals of $\Delta t = 3.6/m_0$ for $L_{\text{asym}} = 28$ and $\Delta t = 16.4/m_0$ for $L_{\text{asym}} = 4$.

At later times the amplitude of the $k \sim k_*$ -modes does not grow any longer, but the ultraviolet end of the spectrum grows extremely rapidly – in fact the occupation number at higher k grows faster than the original growth rate at k_* , as can be observed from the large gaps between the lines in Fig. 7. The final spectrum is shown with a thick line, and its shape fits $f(k) \sim 1/k$ quite well, consistent with a thermal distribution. However, a more detailed inspection of the spectrum shows that the growth of the energy stops before this is reached: the growth stops when the occupation numbers near the lattice cutoff $k/m_0 = \pi/(m_0 a) \approx 10.5$ become appreciable ($\gtrsim 0.05$). After this the distribution just settles towards the thermal one, without increase in energy.

The situation at modest anisotropy (Fig. 7 right) looks quite similar at the beginning. However, in this case the growth in the UV part of the spectrum stops soon after the non-abelian point is reached. The mode spectrum remains dominated by the IR modes, and the total energy grows only approximately linearly with time.

As a check that the occupation number reflects the true distribution of energy over

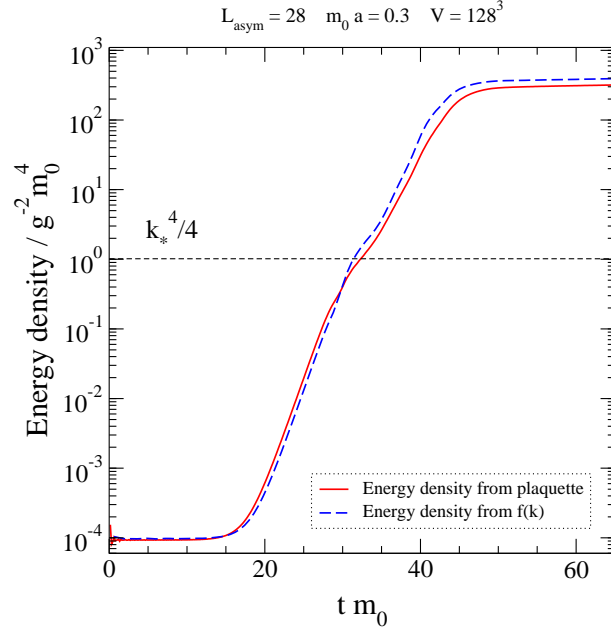


Figure 8: Energy density computed from the Coulomb gauge power spectrum, compared with the true energy density in the magnetic field, for $L_{\text{asym}} = 28$, $m_0 a = 0.3$.

the different modes we compute the total field energy density ε

$$\varepsilon = \int \frac{d^3 k}{(2\pi)^3} |\mathbf{k}| f_s(\mathbf{k}) = \frac{1}{(2\pi)^3} \int_0^\infty dk k^3 f(k), \quad (25)$$

and compare it to the (gauge invariant) direct measurement of the energy from the lattice. The result is shown in Fig. 8. In the weak field regime our measured f slightly over-estimates the energy density. One has to keep in mind that even for very small amplitudes the gauge fields are not free, but are coupled to the W -fields, so that the two curves need not coincide exactly. At large fields the discrepancy is slightly bigger and f yields a slightly too large result. However, the overall disagreement is within a factor of 1.4.

4.3 Average $|\mathbf{k}|$ from gauge invariant operators

The Coulomb gauge occupation numbers strongly indicate that the continued growth seen above is due to population of high momentum modes. However, one may be concerned about gauge artifacts, because strong fields could produce fake high momentum occupancy. Therefore, in order to be certain about our conclusion regarding

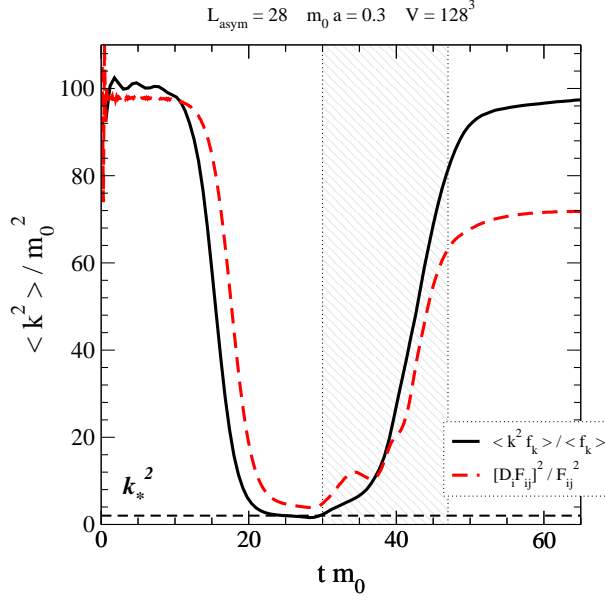


Figure 9: Average \mathbf{k}^2 as a function of time, measured from the gauge fixed occupation numbers $f(k)$, and from the gauge invariant operator, Eq. (26), for the $L_{\text{asym}} = 28$, $m_0 a = 0.3$ -simulation shown in Figs. 7 and 8. The shaded region is the time interval when the non-linear growth of energy is occurring.

the high momentum occupation, it is mandatory to investigate this result also using gauge invariant measurements. A measure for the typical momentum squared of the color-magnetic fields is

$$\langle \mathbf{k}^2 \rangle \equiv \frac{\int \text{tr}(\mathbf{D} \times \mathbf{B})^2 d^3x}{\int \text{tr} \mathbf{B}^2 d^3x} \quad (26)$$

In electrodynamics this would equal

$$\langle \mathbf{k}^2 \rangle_{\text{QED}} = \frac{\int \mathbf{k}^2 |\mathbf{B}(\mathbf{k})|^2 d^3k}{\int |\mathbf{B}(\mathbf{k})|^2 d^3k}$$

In QCD there is also the commutator $[A_i, B_j]$ contributing to $\langle \mathbf{k}^2 \rangle$. So it appears that large $\langle \mathbf{k}^2 \rangle$ does not necessarily imply that the typical \mathbf{k}^2 of the magnetic field is large. However, in the 1-dimensional simulations [15] where the unstable modes grow indefinitely, the commutator terms were found to remain small in accordance with the abelianization picture of Ref. [8]. Thus we expect our $\langle \mathbf{k}^2 \rangle$ to be a good measure of the momentum of the modes. Note in particular that the commutator term

is parametrically of the same size as the gradient term when non-linear effects start playing a role.

In Fig. 9 we show $\langle \mathbf{k}^2 \rangle$ as a function of time, both computed from the gauge invariant object (26) and from the Coulomb gauge occupation numbers. At early times ($t < 12/m_0$), when the fields are very weak, $\langle \mathbf{k}^2 \rangle$ is large because it is dominated by UV modes due to our white noise initial conditions. As soon as the unstable modes start growing they give the dominant contribution to $\langle \mathbf{k}^2 \rangle$ which is then of order k_*^2 . The two curves do not coincide which is not surprising since even for free fields they would in general not be identical. Once one is in the non-linear regime, the average \mathbf{k}^2 increases rapidly. This is a clear signal of a rapid transfer of energy to high momentum field modes. When the lattice cutoff starts having an influence on the time evolution ($tm_0 \gtrsim 45$), the two curves start to deviate strongly.

4.4 Cooling

Another gauge invariant method for obtaining information about the gauge field spectrum at a given physical time is to take the gauge field configuration at that time and let it evolve in the (unphysical) cooling 'time' τ using the equation of motion

$$\partial_\tau A_i = D_j F_{ji} \quad (27)$$

This reduces the gauge field energy monotonously. For weak fields the Fourier components in Coulomb gauge evolve like

$$A_i(\tau, \mathbf{k}) = \exp(-\tau \mathbf{k}^2) A_i(0, \mathbf{k}). \quad (28)$$

Thus, the cooling has the largest effect on the high momentum modes and they are depleted first. Results for the cooling time dependence of the magnetic field energy are shown in Fig. 10 (full lines), measured at intervals $\Delta t = 3.6/m_0$ during the evolution of a system with strong anisotropy ($L_{\text{asym}} = 28$).

For free fields with a thermal spectrum Eq. (28) gives the result $\text{Energy} \sim \tau^{-3/2}$ for large enough τ . This behavior is clearly visible at early time cooling curves, the bottom curves in Fig. 10.⁹ When we are in the linear regime where the unstable modes grow exponentially, practically all of the the energy is in the infrared modes, and the cooling takes more time to have any effect on the total energy. This is visible as horizontal

⁹Our initial condition was small amplitude white noise for \mathbf{E} , which is thermal by itself. This rapidly populates \mathbf{A} -modes to an approximately thermal distribution.

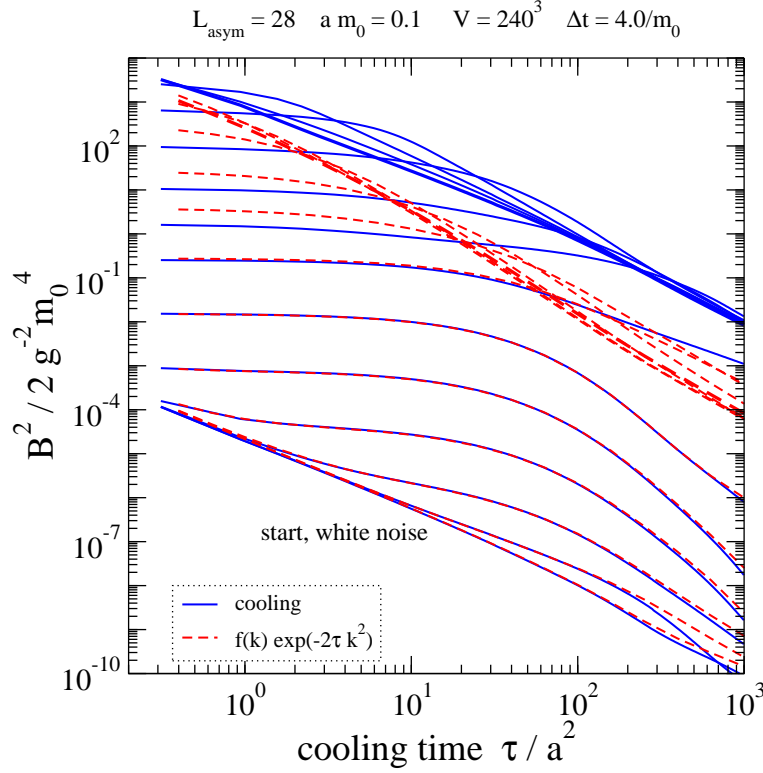


Figure 10: Magnetic field energy (solid lines) during the cooling of the field configurations. The dashed lines are obtained from the ‘cooled’ Coulomb gauge occupation numbers, Eq. (29). The different curves are for physical times in intervals of $4/m_0$, with time increasing from bottom to top. The final curves for both cases are shown with thicker lines.

lines in the middle part of the cooling plot. When the cooling time reaches $\tau \sim 1/k_*^2$, the energy starts to decrease rapidly and the cooling curves develop a smooth shoulder.

The results from the gauge invariant cooling can be directly compared with the Coulomb gauge fixed field mode spectrum. Because $f(|\mathbf{k}|) \propto |\mathbf{A}(\mathbf{k})|^2$, we obtain ‘cooled occupation numbers’ from

$$f_{\text{cool}}(k, \tau) \equiv e^{-2k^2\tau} f(k). \quad (29)$$

From this we can calculate the corresponding energy density as a function of τ . These are plotted in Fig. 10 with dashed lines. We observe that these match the gauge invariant cooling curves perfectly at initial times where the field amplitudes are small.

However, at around $t = 28/m_0$ (7th curve from the bottom, see also Fig. 5) the system enters the non-linear evolution domain and the two curves start to separate.

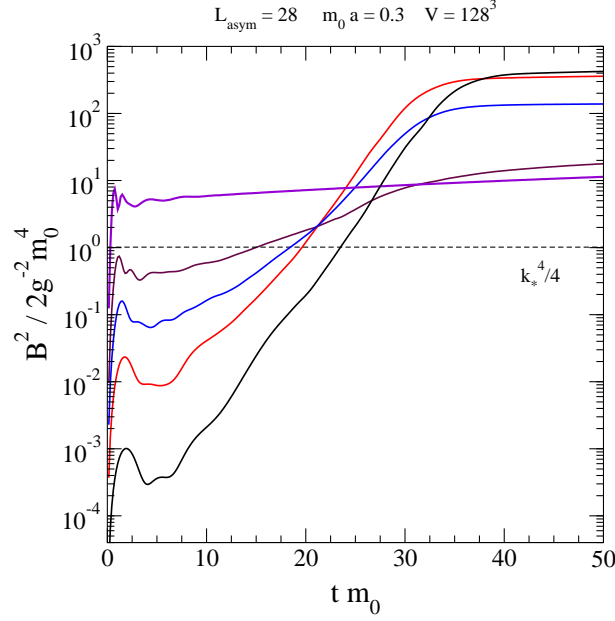


Figure 11: Time evolution of magnetic field energy for different choices of the initial field amplitude.

This is due to two effects: firstly, the gauge fixed occupation number calculates energy slightly incorrectly for large fields, especially in the infrared end of the spectrum. Secondly, for large amplitude fields the non-linear equations of motion make the cooling significantly less efficient in reducing the energy. Thus, in the linear approximation used in Eq. (29) the energy decreases much faster than with the gauge invariant cooling. This is clearly visible in Fig. 10. Nevertheless, the main features are the same: the ‘shoulder’ in the cooling curves moves towards smaller τ , which implies that the ultraviolet modes become occupied.

4.5 Non-weak field initial conditions

So far we have only considered very weak initial fields. With such initial conditions only modes which have \mathbf{k} very close to the z -axis get substantially excited because this is where the growth rate is the largest. By the time the equations of motion become non-linear, the field’s momentum distribution is almost 1-dimensional. It does not mean, however, that our results are just what has been observed in $1 + 1$ dimensional simulations [15], where the growth continues beyond the non-abelian saturation limit.

This is because in our $3 + 1$ dimensional simulations with moderate anisotropy the growth saturates even for very weak field initial conditions (cf. Fig. 4 and Ref. [11]).

Let us now consider larger initial fields (Fig. 11). In this case we use only the strong anisotropy lattices, $L_{\text{asym}} = 28$, and $m_0 a = 0.3$. The electric fields are now initialized with an infrared-dominated spherically symmetric spectrum, $\langle \mathbf{E}(\mathbf{k}) \rangle \propto \exp[-\mathbf{k}^2/(0.6m_0)^2]$. The initial electric field energy densities vary from $0.0032/(g^{-2}m_0^4)$ to $14.1/(g^{-2}m_0^4)$; from the electric field the energy is rapidly pumped in the magnetic fields, as is evident from the figure. Note that the initial momentum spectrum is dominated by modes $k \lesssim k_*$.

We see that there is a very strong dependence on the size of the initial fields. If the fields start out near the non-abelian point (20) there is practically no growth.¹⁰ This behavior is very different from the one observed in Ref. [17] where there is growth for large initial fields. We leave more detailed analysis for further study.

5 Lattice artifacts

When a new phenomenon is studied with lattice simulations, it is very important to quantify possible harmful discretization and finite volume effects. The very large range of scales makes this check especially crucial in this case. As we shall detail below, all lattice effects appear to be well under control.

Lattice spacing: The effects caused by different lattice spacings a were already discussed above. As can be seen from Fig. 4, at weakly anisotropic hard mode distributions the finite a effects are small – the small dispersion of the results is of the same magnitude than statistical deviations at fixed a . We made no effort to enforce physically equivalent initial conditions for different values of a . On the other hand, the finite lattice spacing effects were seen to be quite large for strong anisotropy, Fig. 5, due to the population of the ultraviolet modes. Even in this case there appears to be an universal lattice spacing independent evolution, which finite a simulations follow before they finally saturate.

¹⁰It should be noted that in this case the system is not dominated by single mode $\mathbf{k} \approx k_* \hat{\mathbf{z}}$; thus, the ‘non-abelian limit’ for energy density does not describe the properties of the system as well as before. Nevertheless, we keep this quantity for comparison.

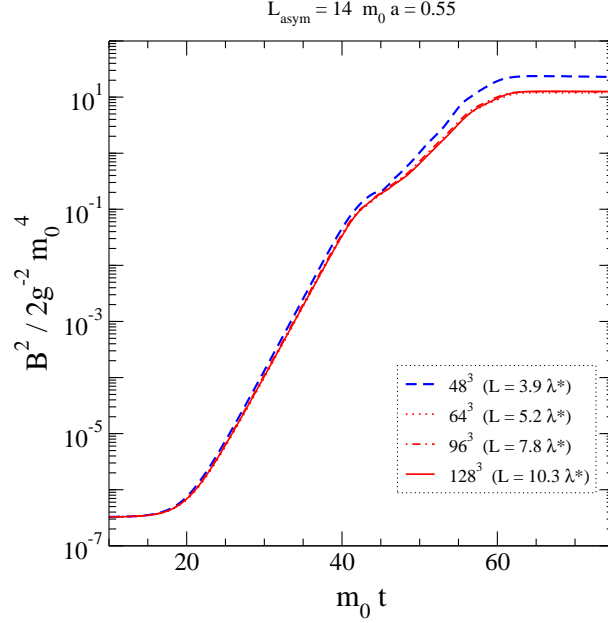


Figure 12: The growth in magnetic energy for $L_{\text{asym}} = 14$, $m_0 a = 0.55$ runs using different volumes. The 3 largest volume curves are practically on top of each other.

Finite volume: If the volume is too small, it can effectively lower the dimensionality of the system. Indeed, too small volume can cause too much growth. In Fig. 12 we show the evolution using 4 different volumes for $L_{\text{asym}} = 14$, $m_0 a = 0.55$ -case. Except for the smallest volume the curves fall on top of each other. (The statistical dispersion between the large volume runs is very small due to the smallness of the random initial fluctuations.) Thus, neither the exponential growth nor the final saturation can be due to the finite size of the system. In general, we require system sizes $L \gtrsim 5(2\pi/k_*)$, except for the very smallest lattice spacing.

Finite L_{max} : We have also studied the L_{max} -dependence of the field growth. In Fig. 13 we show the magnetic energy density evolution for $L_{\text{asym}} = 28$, $m_0 a = 0.3$ on a 128^3 lattice, using $L_{\text{max}} = 32$ and $L_{\text{max}} = 48$. In this case we used identical initial conditions. As can be seen, the evolution is almost identical. (See also Fig. 3.)

Finite δt : In addition to finite lattice spacing a , in simulations of equations of motion one has to check the finite update time-step effects. In this work we used $\delta t = 0.1a$, and checked the stability of the results against $\delta t = 0.05$ simulations with

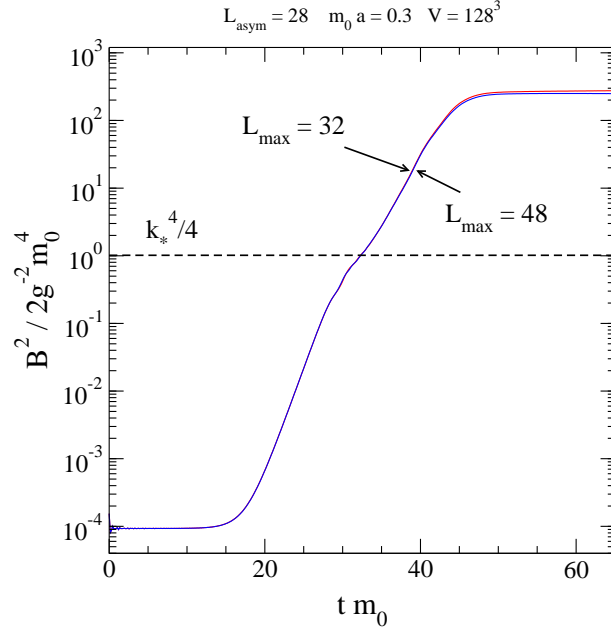


Figure 13: The evolution of the magnetic field energy density for $L_{\text{asym}} = 28$, $m_0 a = 0.3$ -lattices, using L_{max} -cutoffs 32 and 48. The initial conditions were identical for the two runs.

otherwise identical setup. The results are in practice indistinguishable, showing that our original $\delta t = 0.1a$ is sufficiently small.

6 Summary and discussion

We have studied the dynamics of infrared gauge fields in anisotropic $SU(2)$ plasmas in the so called hard loop approximation, i.e., neglecting the backreaction of the infrared gauge fields on the phase space distribution of the high momentum partons. Starting from weak field initial conditions we find a behavior which appears to be qualitatively different from what was observed previously for weakly anisotropic plasmas. The field energy grows until non-linear effects start playing a role, which slow down the growth. But then the growth resumes and appears to continue without limit and it is only stopped by the lattice cutoff. For very strong anisotropy it is almost as fast as the initial exponential growth. This continued growth is different in nature from the linear growth found in weakly anisotropic plasmas.

We have studied gauge fixed occupation, gauge invariant operators and cooling. All

methods indicate that there is a rapid transfer of energy to field modes which have $|\mathbf{k}| \gg k_{\text{max}}$. These are modes which have no instabilities in the weak field regime.

For the largest anisotropy we find a growth rate in the strong field regime which is approximately the same as in the weak field regime. The growth in total energy persists even though the magnitude of the soft gauge modes with $|\mathbf{k}| \sim k_*$ appears to remain constant. The mechanism of the energy transfer from the hard modes (W -fields) to gauge field modes with $|\mathbf{k}| \gg k_*$ remains unknown.

We would like to point out that the earlier 3-dimensional simulations show an interesting structure which has not been discussed so far. After a weak field regime with exponential growth the system enters a phase where the fields become strong and non-linear effects become important. But then, after a brief pause, the fields again start to grow rapidly, almost as fast as during the initial exponential growth. Only after that there is finally a saturation and the subsequent linear growth. To reiterate, even in the weakly anisotropic case there appears to be a 2-stage structure in the saturation. It is conceivable that the behavior we observed is qualitatively similar. However, we find that this continued growth lasts much longer when we increase the anisotropy of the system, maybe forever.

Acknowledgements The work of DB was supported in part through the DFG funded Graduate School GRK 881. KR has been partially supported by the Academy of Finland grants 104382 and 114371. The simulations in this work have been made at the Finnish IT Center for Science (CSC, Espoo, Finland).

References

- [1] See the discussion in K. Adcox *et al.* [PHENIX Collaboration], *Formation of dense partonic matter in relativistic nucleus nucleus collisions at RHIC: Experimental evaluation by the PHENIX collaboration*, Nucl. Phys. A **757** (2005) 184 [arXiv:nucl-ex/0410003].
- [2] For a review see e.g. A. H. Mueller, *Parton saturation at small x and in large nuclei*, Nucl. Phys. B **558** (1999) 285 [arXiv:hep-ph/9904404].
- [3] S. M. H. Wong, “Thermal and chemical equilibration in a gluon plasma,” Nucl. Phys. A **607**, 442 (1996) [arXiv:hep-ph/9606305].

- [4] A. H. Mueller, *Toward equilibration in the early stages after a high energy heavy ion collision*, Nucl. Phys. B **572** (2000) 227 [arXiv:hep-ph/9906322].
- [5] J. Bjorker and R. Venugopalan, “From colored glass condensate to gluon plasma: Equilibration in high energy heavy ion collisions,” Phys. Rev. C **63** (2001) 024609 [arXiv:hep-ph/0008294].
- [6] R. Baier, A. H. Mueller, D. Schiff, D. T. Son, ‘*Bottom-up*’ *thermalization in heavy ion collisions*, Phys. Lett. B **502** (2001) 51 [arXiv:hep-ph/0009237].
- [7] S. Mrowczynski, *Plasma instability at the initial stage of ultrarelativistic heavy ion collisions*, Phys. Lett. B **314** (1993) 118.
- [8] P. Arnold and J. Lenaghan, *The abelianization of QCD plasma instabilities*, Phys. Rev. D **70** (2004) 114007 [arXiv:hep-ph/0408052].
- [9] P. Arnold, J. Lenaghan, G. D. Moore and L. G. Yaffe, *Apparent thermalization due to plasma instabilities in quark gluon plasma*, Phys. Rev. Lett. **94** (2005) 072302 [arXiv:nucl-th/0409068].
- [10] P. Arnold, J. Lenaghan and G. D. Moore, *QCD plasma instabilities and bottom-up thermalization*, JHEP **0308** (2003) 002 [arXiv:hep-ph/0307325].
- [11] P. Arnold, G. D. Moore and L. G. Yaffe, *The fate of non-abelian plasma instabilities in 3+1 dimensions*, Phys. Rev. D **72** (2005) 054003 [arXiv:hep-ph/0505212].
- [12] A. Rebhan, P. Romatschke and M. Strickland, *Dynamics of quark-gluon plasma instabilities in discretized hard-loop approximation*, JHEP **0509** (2005) 041 [arXiv:hep-ph/0505261].
- [13] P. Arnold and P. S. Leang, *Lessons from Non-Abelian Plasma Instabilities in Two Spatial Dimensions*, arXiv:0704.3996 [hep-ph].
- [14] D. Bödeker, *The impact of QCD plasma instabilities on bottom-up thermalization*, JHEP **0510** (2005) 092 [arXiv:hep-ph/0508223].
- [15] A. Rebhan, P. Romatschke and M. Strickland, *Hard-loop dynamics of non-Abelian plasma instabilities*, Phys. Rev. Lett. **94** (2005) 102303 [arXiv:hep-ph/0412016].
- [16] P. Arnold and G. D. Moore, *QCD plasma instabilities: The nonabelian cascade*, Phys. Rev. D **73** (2006) 025006 [arXiv:hep-ph/0509206].

- [17] A. Dumitru, Y. Nara and M. Strickland, *Ultraviolet avalanche in anisotropic non-Abelian plasmas*, arXiv:hep-ph/0604149.
- [18] U. W. Heinz, *Kinetic Theory For Nonabelian Plasmas*, Phys. Rev. Lett. **51** (1983) 351.
- [19] S. Mrowczynski, *Kinetic Theory Approach To Quark - Gluon Plasma Oscillations*, Phys. Rev. D **39** (1989) 1940.
- [20] P. Romatschke and R. Venugopalan, *The unstable Glasma*, Phys. Rev. D **74** (2006) 045011 [arXiv:hep-ph/0605045].
- [21] D. Bödeker, G. D. Moore and K. Rummukainen, *Chern-Simons number diffusion and hard thermal loops on the lattice*, Phys. Rev. D **61** (2000) 056003 [arXiv:hep-ph/9907545].
- [22] S. Mrowczynski, *Plasma instability at the initial stage of ultrarelativistic heavy ion collisions*, Phys. Lett. B **314** (1993) 118.
- [23] P. Arnold and G. D. Moore, *“The turbulent spectrum created by non-Abelian plasma instabilities*, Phys. Rev. D **73** (2006) 025013 [arXiv:hep-ph/0509226].